Scientific Research Publishing

Journal of High Energy Physics, Gravitation and Cosmology, 2023, 9, 1237-1258
https://www.scirp.org/journal/jhepgc
ISSN Online: 2380-4335
ISSN Print: 2380-4327

Relativistic Supernova Blast Waves Exhibit Properties of Gravitational Lenses and the Hubble Constant

Paul Marko

Electromagnetic Design Group, Deerfield Beach, USA
Email: pmarko@aemdgroup.com

How to cite this paper: Marko, P. (2023) Relativistic Supernova Blast Waves Exhibit Properties of Gravitational Lenses and the Hubble Constant. *Journal of High Energy Physics, Gravitation and Cosmology*, **9**, 1237-1258.
https://doi.org/10.4236/jhepgc.2023.94087

Received: July 24, 2023
Accepted: October 28, 2023
Published: October 31, 2023

Abstract

Simulations based on Supernova (SN) observations predict several galactic SN explosions (SNe) can occur every century. Unlike SNes within the Interstellar Medium (ISM) where ambient gas generally absorbs blast waves within a million years, SNes occurring in a rarified environment outside of the ISM generate blast waves which remain in a relativistic free expansion phase for more extended periods. The SN blast wave forms an expanding spherical shell and when multiple blast waves intersect, the overlapping region naturally takes the form of a ring, an arc, or an Einstein Cross structure. The analysis shows the relativistic plasma establishes a medium with permeability which drives the index of refraction greater than 1. As a result, when a shock discontinuity forms in the overlapping region, light is reflected from the host galaxy which exposes the intersecting blast wave regions. The expanding shells are shown to induce an achromatic redshift to the reflected light consistent with those measured for gravitational lenses. Further, it is shown that a Hubble equation for a blast wave around the Milky Way Galaxy can be parameterized to approximate measured redshifts over a wide range of distances.

Keywords

Supernova, Plasma, Gravitational Lens, Einstein Cross, Hubble Constant

1. Introduction

Ongoing technical advances in sensors, telescopes and light processing algorithms are enabling cosmic observations with higher image clarity, wider bandwidth and better spectrum resolution. These advances continue to expose additional details prompting the development of new or refined models and theories to better align with the data. In general, objects appearing in the light field have

been accepted as being present at or near the observed position in space with changes to the light spectrum rest frequency credited to Doppler shifts from peculiar velocity and cosmic expansion. Described here, if the media refractive index between a light source and observer is changing during a measurement, the intervening media can induce shifts in the observed rest frequency. Identification of a cosmic media capable of generating a dynamic refractive index effect focuses on a class of Supernova explosions (SNes) in the rarified Circumgalactic Medium (CGM) or Intergalactic Medium (IGM). A literature review lends support to this class of explosions, as large populations of stars are known to reside outside the Interstellar Medium (ISM) and observations of galactic matter do not reveal any inconsistencies. The SN blast wave, modeled as an ionized plasma, travels at relativistic velocity for extended periods and produces magnetic fields shown to drive the index of refraction above 1. This occurs during the period a charged particle interacts with a passing photon soliton where the particle movement introduces an asymmetric magnetic field within the interaction region which generates a bias in-phase with the photon magnetic field. The Effective Medium Theory is leveraged to compute the resulting permeability. The blast wave forms a media in the shape of an expanding spherical shell and where multiple blast waves intersect, a shock interface, if formed, can induce reflections to EM waves. As a result, host galaxy reflections off these discontinuities form rings, arcs or Einstein Cross structures and when modeled with appropriate medium properties exhibit magnitudes and redshifts consistent with gravitational lenses. A Hubble equation derived for incoming extragalactic light fields interacting with an expanding blast wave around the galaxy is shown to induce an apparent recession velocity comparable with Hubble Constant measurement campaigns over a wide range of distances.

2. Dynamic Index of Refraction and Redshift

An expression can be derived for the frequency observed when a media with refractive index $\eta > 1$ is expanding in the light path by referencing **Figure 1**.

In **Figure 1**, the wedge with refractive index $\eta_1 > 1$ is moved perpendicular to the light path as shown with velocity v in m·s^{-1}. While in motion, along the observation path the wedge is displacing media $\eta_0 = 1$ with $\eta_1 > 1$ media. The velocity v_w at which the dielectric wedge width is growing along the observation path is

$$v_w = v * TAN\,\alpha \tag{1}$$

where α is the angle of the wedge leading edge. The net shift in the emission frequency f_{emit} can be determined by first calculating the frequency at the interface exiting the wedge f_{int} as it expands along the observation path and then the observed frequency. The relationship between the observed frequency f_{obs} and the emission frequency f_{emit} is given by

$$f_{obs} = \left(\frac{c - v_w\eta_1}{c - v_w\eta_0}\right) f_{emit}\,. \tag{2}$$

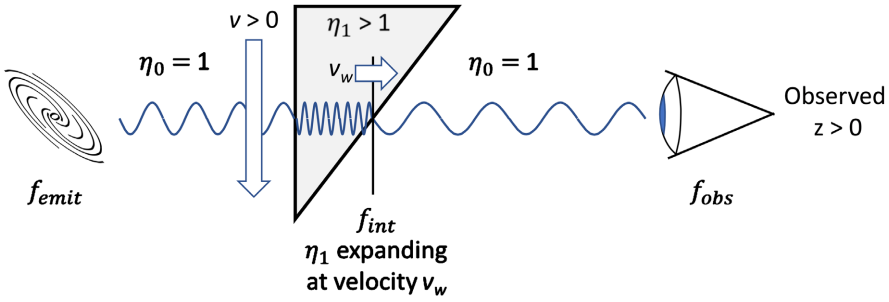

Figure 1. A redshift z is induced between stationary end points during a refractive index change. Refractive index of the propagation path is increasing as the wedge ($\eta_1 > 1$) is expanding along the line of sight. With the wedge moving as shown the redshift present at the wedge interface (f_{int}) receding from the emitter exceeds the blueshift from the wedge interface approaching the observer resulting in a net redshift along the observation path.

The redshift z is defined as

$$z = \frac{f_{emit} - f_{obs}}{f_{obs}}. \tag{3}$$

Equations (2) and (3) show when $v_w > 0$ and $\eta_1 > \eta_0$ a net redshift will be present along the observation path. When the wedge stops moving with $v_w = 0$ the redshift returns to zero. When $v_w = 0$, moving the wedge laterally along the observation path does not induce a redshift. The redshift z in terms of refractive index η_1 with $\eta_0 = 1$ can be expressed as

$$z = \frac{v_w \cdot (\eta_1 - 1)}{c - v_w \cdot \eta_1}. \tag{4}$$

3. Supernova Blast Waves and Expansion Medium

Most of what is known and theorized about the SNe comes from photometric observations. To a good approximation, the exploding material on the SN can be modeled as a fully ionized plasma [1]. Theoretical hydrodynamic explosion models for Type Ia SN have been developed based on observed light curves and spectra. While the models predict early phase ejecta velocities range from less than 100 km·s^{-1} to over 25,000 km·s^{-1}, multiple models predict a high density of ejecta material tightly grouped near 10,000 km·s^{-1} [2].

For an SNe within the ISM, the expanding ejecta is segmented into multiple phases as it interacts with the surrounding media [3]. This interaction begins when the SN ejecta moves radially outward at velocities in the range of 10^4 km·s^{-1} in the form of a pressure pulse which transitions to a shock wave when it encounters gas in the Circumstellar Medium (CSM) and ISM. The shock wave is characterized by a discontinuity in pressure which propagates through the gas and for simplicity can be modeled with a Friedlander waveform [4] described by

$$P(t) = P_s e^{\frac{-t}{t_a}} \left(1 - \frac{t}{t_a}\right) \tag{5}$$

where $P(t)$ is the pressure versus time at a point in space, P_s is the overpressure and t_a is the time it takes for the overpressure to return to ambient pressure, shown in Figure 2 as a function of distance.

Referring to Figure 2, the behavior of the plasma across the discontinuity is defined by a set of jump conditions which constrain the fluid parameters and EM parameters to conserve mass, momentum, and energy [5]. The width of the blast wave in Figure 2 is defined here as the radial length the overpressure region remains above ambient pressure. As the blast wave expands with time, the width also expands at velocity v_w (analogous to v_w in Figure 1), due to variations in particle velocity and other factors discussed later.

Based on observations of galaxy clusters, large populations of stars exist outside of the ISM and form luminous halos which extend hundreds of parsecs around the galaxy. The flux of the intracluster light given off by these halos has been measured in the range of 6% - 22% of the total cluster light [6] [7]. Tidal stripping and three body interactions are known processes which drive stars into the IGM. In spiral galaxies, hydrodynamic simulations support the height of the SNe relative to the ISM is a major factor impacting the SNe-driven outflow [8]. When a SN explodes outside the ISM, referred to as a remote SN (RSN) hereafter, as the blast wave leaves the CSM and propagates in a rarified galactic medium, it remains in the high velocity free expansion phase for an extended period. The RSN's relativistic blast wave (RBW) energy converted to heat during the early phase rapidly cools as the blast wave expands at a velocity in the range of 10,000 km·s^{-1}. While RBWs expanding into the rarified CGM are generally not observable due to 1) the low rate of occurrence reduces early phase detections, 2) the plasmas rapidly cool, are optically thin and non-emissive, 3) the propagation medium is too thin to generate a detectable radio emission and 4) the plasma density is too low for detection by absorption spectroscopy, extensive observational data on galactic halos and the CGM do not rule out their existence.

As the RBW expands in the IGM largely unimpeded, the leading-edge pressure discontinuity can gradually soften and transition back to a pressure pulse

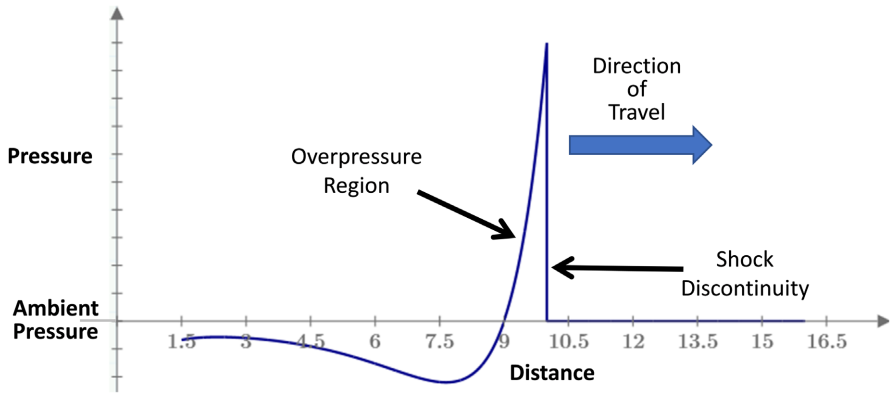

Figure 2. Plot shows SNBW pressure versus distance. The shock discontinuity forms in ambient gas when the higher-pressure portion of the pressure pulse catches up with the slower moving leading edge causing the leading edge to steepen.

which diminishes any observable EM wave reflections associated with the difference between the refractive index of the blast wave plasma and the ambient media. In this case the reflection from the blast wave is similar to a reflection in a transmission line, where if an impedance discontinuity occurs along the transmission path some energy will be reflected and some transmitted in close approximation with the reflection coefficient Γ_r, where

$$\Gamma_r = \frac{Z_2 - Z_1}{Z_2 + Z_1}. \tag{6}$$

This equation is applicable to the blast wave where the incident EM wave travels from a media with characteristic impedance Z_1 to a media with characteristic impedance Z_2 with the sign of the result describing the phase of the reflected energy.

Tapering the transmission line at the interface to introduce a more gradual impedance transition is a common technique used to reduce reflections and minimize transmission losses [9]. In a blast wave propagating with a continuous tapered pressure profile, with the exception of refractive bending it can be shown EM waves will pass largely transparently through the blast wave including the condition where the plasma refractive index substantially differs from free space.

4. High Velocity Plasma Refractive Index

The refractive index η for EM radiation can be expressed

$$\eta = \sqrt{\epsilon_r \mu_r} \tag{7}$$

where ϵ_r is the media's relative permittivity and μ_r is the media's relative permeability. For transverse electromagnetic waves in a simple dielectric plasma the relative permittivity can be expressed

$$\epsilon_r = 1 - \frac{\omega_{pe}^2}{\omega^2} \tag{8}$$

where ω_{pe} is the electron plasma frequency and ω is the electromagnetic wave frequency [10]. For light frequencies, $\omega \gg \omega_{pe}$ and ϵ_r approaches 1. In a uniform high-velocity plasma, the magnetic fields associated with the individual particles interact with the EM wave and drive up the permeability. For a thin high velocity plasma, the permeability is calculated based on the Effective Medium Theory, where the macroscopic electrodynamic properties of the medium are determined based on the microscopic fields associated with the charged particle interaction with the individual photons. The Effective Medium Theory for non-resonant particles can be expressed as

$$\mu_{eff} = A\mu_1 + (1 - A)\mu_0 \tag{9}$$

$$\text{with} \quad A = \frac{\pi D^2 b}{4a^2 H} \tag{10}$$

where μ_{eff} is the permeability of the composite medium, μ_1 is the permeability in the photon interaction area with the electron, μ_0 is the permeability of

the medium between the electrons, the term $\pi D^2 b$ is the volume of a cylinder encompassing the photon-electron interaction area and the term $a^2 H$ is the average volume of free space surrounding the charged particle as defined by the inverse of the particle density [11]. The photon-electron interaction area approximates the photon soliton ellipsoid with a cylinder of radius $D = \frac{\lambda}{2\pi}$ and height $b = \lambda_{eff}$ [12], where $\lambda_{eff} = \frac{\lambda}{\eta_{eff}}$ and η_{eff} are the effective wavelength and refractive index in the medium applicable to the direction of photon propagation.

From Equations (7) and (9), the plasma effective refractive index η_{eff} with $\epsilon_r = 1$ is then

$$\eta_{eff} = \sqrt{\mu_{r\_eff}} \tag{11}$$

where $\mu_{r\_eff} = \mu_{eff} / \mu_0$.

For the microscopic field calculations, the total composite average magnetic flux density B_t within the photon-matter interaction area where the photon passes a charged particle is defined as

$$B_t = \mu_r \mu_0 H_{pavg} = B_{lavg} + \mu_0 H_{pavg} \tag{12}$$

where μ_r is the relative permeability of the photon interaction with the charged particle. The term $\mu_0 H_{pavg}$ is the average photon flux density where H_{pavg} is the photon magnetic field intensity in A/m. The term B_{lavg} is the sum of the averaged non-photon magnetic flux densities correlated to the phase of the photon magnetic field. When the interaction is evaluated in proximity to a galaxy, B_{lavg} is expressed as

$$B_{lavg} = B_{e\_i} + B_{gc} + B_{e\_bw} + B_{ap} \tag{13}$$

where B_{e_i} is the average electron flux density from the velocity induced by the composite galactic core field, B_{gc} is the average flux density from the galactic core, B_{e_bw} is the average electron flux density induced by blast wave velocity and B_{ap} is the summation of the average flux densities from adjacent particles which can be neglected in low density plasmas. It can be shown that B_{e_bw} is the dominant contributor to B_{lavg} and other flux density sources can be neglected. Rearranging equation (12) and substituting $B_{pavg} = \mu_0 H_{pavg}$, μ_r in the photon interaction area can be expressed

$$\mu_r = \frac{B_{e\_bw}}{B_{pavg}} + 1 \tag{14}$$

where B_{e_bw} and B_{pavg} are values averaged over a wavelength.

4.1. Electron Flux Density Induced by Blast Wave Velocity, B_{e_bw}

The average electron flux density induced by the blast wave velocity B_{e_bw} is computed based on the diagram in **Figure 3**, where the shaded region represents the photon soliton interaction region defined previously.

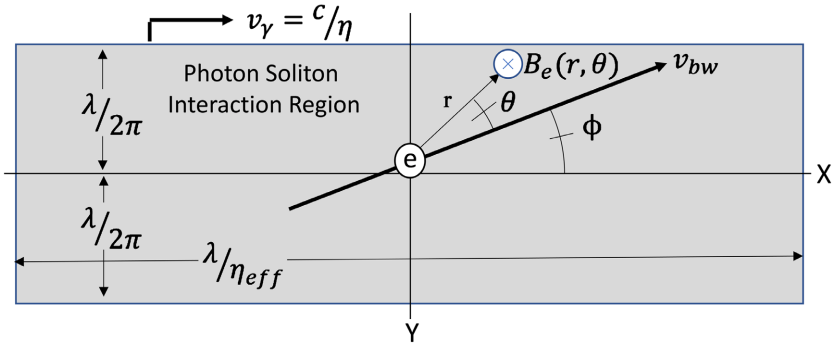

Figure 3. Plot shows the photon soliton interaction region as it travels along the x-axis and passes through the high velocity electron magnetic field.

The interaction region is modeled as a cylinder encompassing the photon traveling from left to right with axis of symmetry along the x-axis which lies on a radial from the photon source (not shown). The electron travels with velocity v_{bw} with angle ϕ with respect to the photon velocity as shown. The magnetic field of the electron within the interaction region is evaluated only when the electron is within the interaction region.

For an electron traveling with velocity $\boldsymbol{v}_{bw}$ the magnetic flux density around the electron is approximated by

$$\boldsymbol{B}_e(r,\theta) \approx \frac{\mu_0}{4\pi}\frac{q}{r^2}\left(\boldsymbol{v}_{bw} \times \hat{\boldsymbol{r}}\right) \tag{15}$$

where q is the charge, $\boldsymbol{v}_{bw}$ is the electron velocity vector, r is the distance from the electron to the position of $\boldsymbol{B}_e$, $\hat{\boldsymbol{r}}$ is the unit vector from the electron to $\boldsymbol{B}_e$ and θ is the angle of $\hat{\boldsymbol{r}}$ relative to $\boldsymbol{v}_{bw}$.

For determining the average electron magnetic flux density correlated to the photon magnetic field, the photon/electron interaction begins at time $t = 0$ with the photon traveling at velocity $c_{eff} = \dfrac{c}{\eta_{eff}}$ and the electron traveling at velocity v_{bw} with the photon interaction area positioned along the x-axis between $x = 0$ and $x = \lambda_{eff}$ and the electron positioned at $x = \lambda_{eff}$, $y = 0$ (not shown). The photon/electron interaction ends at time $t = \dfrac{\lambda_{eff}}{c_{eff} - v_{bw}\cos(\phi)}$ with the photon interaction area positioned between $x = \lambda_{eff}\left(1 + \dfrac{v_{bw}\cos(\phi)}{c_{eff} - v_{bw}\cos(\phi)}\right)$ and $x = \lambda_{eff}\left(2 + \dfrac{v_{bw}\cos(\phi)}{c_{eff} - v_{bw}\cos(\phi)}\right)$ which is where the photon/electron interaction area passes the electron (not shown). The average electron magnetic flux density as a function of time t and position x can be calculated by averaging along the y-axis as expressed by

$$B_{e\_bwy}(t,x) = \frac{\pi}{\lambda}\int_{-\frac{\lambda}{2\pi}}^{\frac{\lambda}{2\pi}} \frac{\mu_0 q_e v_{bw}}{4\pi\left(\left(x'\right)^2 + \left(y'\right)^2\right)} \sin\left(\operatorname{atan}\left(\frac{y'}{x'}\right) - \phi\right) \mathrm{d}y \tag{16}$$

where $x' = x - \left(\lambda_{eff} + v_{bw} \cdot t \cdot \cos(\phi)\right)$, $y' = y - v_{bw} \cdot t \cdot \sin(\phi)$ and with constraints applied to insure the distance to the electron does not drop below 10^{-14} m and $\sin\left(\text{atan}\left(\frac{y'}{x'}\right) - \phi\right)$ returns the correct angle in all 4 quadrants. The flux density at an instant in time can then be averaged over the photon while correcting for the phase of the photon magnetic field by

$$B_{e\_bwxy}(t) = \frac{1}{\lambda_{eff}} \int_{c_{eff} \cdot t}^{c_{eff} \cdot t + \lambda_{eff}} B_{e\_bwy}(t, x) \psi'\left(x - c_{eff} \cdot t\right) \mathrm{d}x \tag{17}$$

where

$$\psi'(x) = \begin{cases} 0 & \text{if } x < 0 \text{ or } x > \lambda_{eff} \\ -1 & \text{if } \sin\left(2\pi \frac{x}{\lambda_{eff}}\right) > 0 \\ 1 & \text{if } \sin\left(2\pi \frac{x}{\lambda_{eff}}\right) < 0 \\ 0 & \text{if } \sin\left(2\pi \frac{x}{\lambda_{eff}}\right) = 0 \end{cases} \tag{18}$$

The electron magnetic flux density averaged over the period of photon/electron interaction is then given by

$$B_{e\_bw} = \frac{c_{eff} - v_{bw} \cdot \cos(\phi)}{\lambda_{eff}} \int_0^{\frac{\lambda_{eff}}{c_{eff} - v_{bw} \cdot \cos(\phi)}} B_{e\_bwxy}(t) \mathrm{d}t. \tag{19}$$

As the photon passes the electron, if the electron were to remain in a fixed position relative to the radial axis ($y = 0, \phi = 0$), the averaged electron magnetic flux density in the interaction region would be negligible. With $\phi \neq 0$, the electron moves across the photon radial axis as it passes and the asymmetry of the magnetic flux density versus time creates a significant average flux density as a function of the electron velocity and the angle ϕ.

4.2. Photon Flux Density, B_{pavg}

The average photon magnetic field intensity H_{pavg} in the interaction area is computed based on the EM wave intensity $I_{\gamma s}$ from a continuous photon stream. If the power from the photon stream source is $P_{\gamma s}$, the intensity at distance R from the source is given by

$$I_{\gamma s} = \frac{P_{\gamma s}}{4\pi R^2}. \tag{20}$$

The peak magnetic field intensity H_{pmax} is defined by

$$H_{pmax} = \sqrt{\frac{2 \cdot I_{\gamma s}}{\eta_{eff} \cdot Z_0}}, \tag{21}$$

where $Z_0 = 377$ ohms is the intrinsic impedance of free space. The average

photon magnetic flux density B_{pavg} is then given by

$$B_{pavg} = \frac{2\mu_0}{\lambda_{eff}} \int_0^{\frac{\lambda_{eff}}{2}} H_{pmax} \sin\left(2\pi \frac{x}{\lambda_{eff}}\right) \mathrm{d}x \,. \tag{22}$$

5. Overlapping RBW Structures as Gravitational Lenses

Gravitational lenses are widely observed in the universe and are theoretically formed when light from a distant galaxy passes near to a foreground galaxy with a gravitational field that bends the light path. Free expanding RBWs can appear as a gravitational lens if appropriate plasma properties and environmental conditions impacting the refractive index are present.

Consider the case of two free expanding RBWs originating from two largely separated points in a galaxy, as depicted in Figure 4. In the overlapping region, the angle between the velocity vectors establishes the magnitude of the differential velocity vector which plays a key role in determining whether or not a shock discontinuity will form. At low acute angles the delta in velocity may not exceed the Alfven and sound speeds of the plasma and a shock condition may not be present. For higher acute angles, whether or not the shock conditions are met, the overlapping region can exhibit more complex behavior such as time dependent rotations of the planes of the magnetic fields and while the nature of such shocks is not fully understood [13], the shock discontinuity, if formed, can be modeled as surfaces at the leading edge of each RBW.

The shock surfaces from the overlapping RBWs shown in Figure 4 form a semicircle and reflect light from the host galaxy exposing the underlying structure. Since the reflecting surfaces are slices from an RBW hemisphere, the focal point for a distant observer is approximately 1⁄2 the RBW hemisphere radius towards the center and moves as the circular reflective surface is traversed. An extended arc of reflected light is effectively sourced from different portions of the host galaxy and can highlight the brightness patterns in an underlying spiral pattern.

The light spectrum measured from these ring structures exhibits an additional

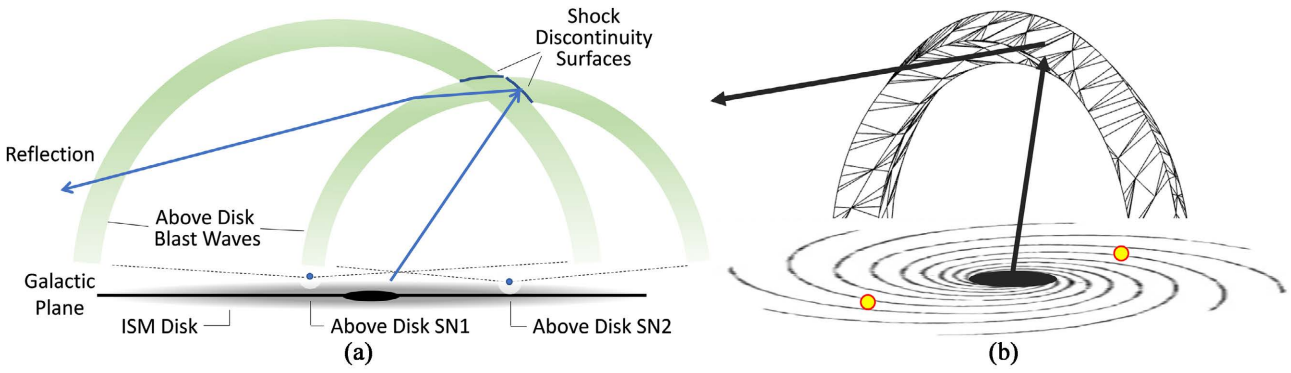

Figure 4. Depiction of the intersection of RBWs. (a) Blast waves are shown in green from SN1 and SN2 positioned apart in the galaxy intersect and form shock surfaces. Light from the galaxy can reflect off the shock discontinuity in the intersecting region. (b) Perspective view of the intersecting blast waves appearing as a partial ring.

redshift with respect to light from the host galaxy [14] [15], implying the overlapping RBWs introduce a redshift. How this redshift occurs is described by first focusing on a single RBW. Assume the RBW were to expand from an initial width of 0.6 light days, based on 20 days of ejecta traveling at 0.025 C after CSM interaction [4] [16], to a width of 5 k light years over a 2-million-year period due to differences in initial particle velocity, changes in particle velocity induced by swept up matter and radial dispersion. If linear expansion is assumed for the width, the expansion rate is approximately 0.0025 light years per year which equates to a velocity v_w = 750 km·s^{-1}. Although not included here, particle interaction in overlapping region is also expected to significantly contribute to the width expansion velocity downstream of the leading edge.

The expanding width of an RBW induces a redshift in a manner analogous to a wedge moving into the light path as described previously.

5.1. Plasma Permeability for Photons Sourced from Galactic Core

Figure 5 shows a simplified SNe arrangement for deriving the electrical properties of a reflection from the shock interface. In Figure 5(a), the RBWs from SN1 and SN2 have expanded to outer radii of 50 K LY and 40 K LY and intersect at an approximate 75 degree angle 35 K LY above the galactic core. Light from the galactic core reflects off the shock interface which appears as an arc to a distant observer.

Figure 5(b) is a perspective view from the direction of the observer. The analysis will initially focus on the reflection from a 30 degree arc sourced from the stars in the galactic core using typical Milky Way Galaxy parameters of core radius $R_{core} = 13$ K LY and core luminosity $L_{core} = 2.5\times10^{10} L_{\odot}$ [17]. As shown, the electrons within the arc will be primarily illuminated from the core stars, which for simplicity can be modeled with a total of 2.5 × 10^{10} stars, each with luminosity $L_{\odot}$, distributed over a 26 K LY diameter disc spaced 35 K LY away.

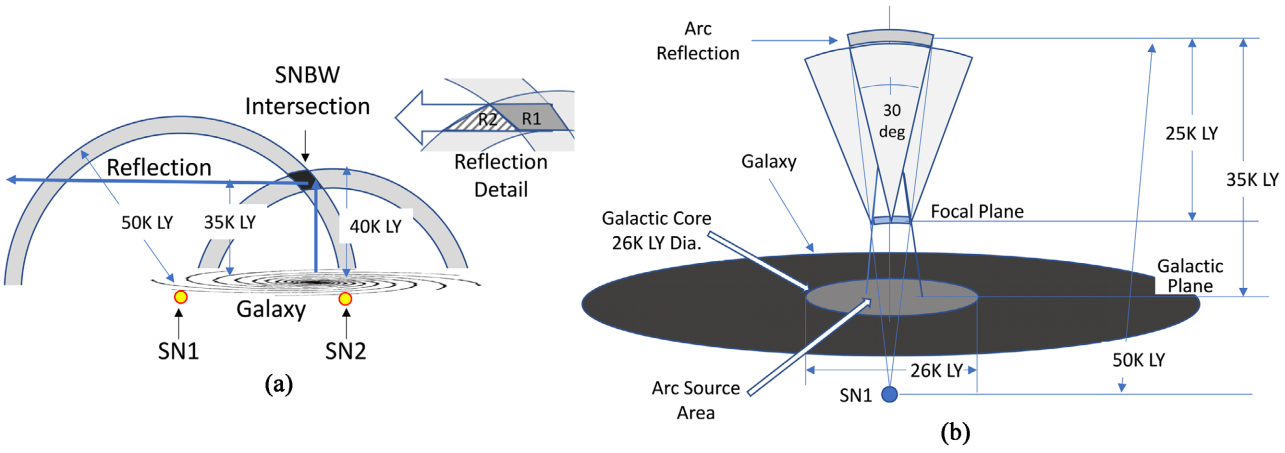

Figure 5. Diagram of the SN Plasma Interaction with the EM Wave. (a) Overlapping blast wave diagram with plasma regions influencing the reflection redshift shown. (b) Perspective diagram from the direction of the observer showing the overlapping arc segment above the galaxy.

For the particle density in the RBWs assume the mass of ejecta from each SNe is equal to $1M_{\odot}$. If the average atomic weight A_r of the ejecta ions is estimated at 16, the total number of ions N_i and electrons N_e if singly ionized is given by

$$N_e = N_i = \frac{M_{\odot} \times N_A}{A_r} = 7.5 \times 10^{55} \tag{23}$$

where $M_{\odot}$ is expressed in grams and N_A is Avogadro's Number.

The volume occupied by the plasma is computed for two spherical shell sizes, a first extending from a radius of 45 K Light Years (LY) to 50 K LY and a second extending from a radius of 35 K LY to 40 K LY. The first shell occupies a volume Vol_{BW50} of 1.2 × 10^{62} m^3 and the second shell occupies a volume Vol_{BW40} of 7.5 × 10^{61} m^3. The electron density e_{dens} from the SNes in $N_e \cdot m^{-3}$ is given by

$$e_{dens} = \frac{N_e}{Vol_{BW}}, \tag{24}$$

where for outer radius 50 K LY $e_{dens50} = 6.2 \times 10^{-7} N_e \cdot m^{-3}$ and for outer radius 40 K LY $e_{dens40} = 1.0 \times 10^{-6} N_e \cdot m^{-3}$ combining for a density of $e_{dens4050} = 1.62 \times 10^{-6} N_e \cdot m^{-3}$ where the shells overlap.

Since the electrons from SN1 and SN2 are crossing the photon path from the galactic center at different angles, B_{e_bw} is computed for each SN.

Substituting $\lambda = 6.57 \times 10^{-7}$ m, $\mu_0 = 4\pi \times 10^{-7}$ H·m^{-1}, $q_e = 1.6 \times 10^{-19}$ C, $\phi = \frac{\pi}{4}$ rad for SN1, $\phi = \frac{\pi}{6}$ rad for SN2, $v_{bw} = 8 \times 10^6$ m·s^{-1} into Equations (16)-(19) yields $B_{e\_bw1} = 5.8 \times 10^{-7}$ T for SN1 and $B_{e\_bw2} = 4.0 \times 10^{-7}$ T for SN2. The average B_{e_bw} is computed using the electron density as a weighting factor with

$$B_{e\_bw} = \frac{e_{dens50}}{e_{dens40} + e_{dens50}} B_{e\_bw1} + \frac{e_{dens40}}{e_{dens40} + e_{dens50}} B_{e\_bw2} = 4.7 \times 10^{-7} \text{ T} \tag{25}$$

To compute the average photon magnetic flux density B_{pavg}, the peak photon magnetic field intensity H_{pmax} in the overlapping region sourced from a coherent EM wave emanating from the galaxy core is first determined. For simplicity, it is assumed that the luminosity from the galaxy core is focused at the *Hα* frequency 4.57 × 10^{14} Hz, where the power of a continuous photon stream is $P_{\gamma s} = 1.38 \times 10^{-4}$ W. With a distance to the galaxy core of approximately 35 K light years, based on Equations (20) and (21), the photon EM wave intensity and peak magnetic field intensity in the overlapping region are $I_{\gamma s} = 1.00 \times 10^{-46}$ W·m^{-2} and $H_{pmax} = 7.29 \times 10^{-25}$ A·m^{-1}. From Equation (22), the average photon magnetic flux density yields $B_{pavg} = 5.83 \times 10^{-31}$ T.

With these values for B_{e_bw} and B_{pavg}, the relative permeability in the photon/electron interaction area based on Equation (14) is $\mu_r = 8.1 \times 10^{23}$. By similarity, the positive charged ions traveling with the electrons will exhibit a relative permeability of $\mu_r = -8.1 \times 10^{23}$. With μ_r negative and the relative permittivity $\epsilon_r = 1$, the refractive index $\eta = \sqrt{\epsilon_r \mu_r}$ will be an imaginary value, where

the photon will be subjected to attenuation or extinction α as a function of distance x according to

$$\alpha(x) = \mathrm{e}^{-\frac{4\pi\eta x}{\lambda}} \tag{26}$$

and will not significantly contribute to the plasma permeability computed for the photon EM field propagating through the medium. As computed at Equation (24), the overlap region will have an electron density of $1.62\times10^{-6}\,N_e\cdot\mathrm{cm}^{-3}$ and with an equivalent number of ions inducing negative permeability, the column density of these ions in the 5 K LY overlap region will be $7.7\times10^{9}\,N_i\cdot\mathrm{cm}^{-2}$. As the observed extinction for neutral hydrogen has been characterized as

$$A(V)/N_H = 5.3\times10^{-22}\ \mathrm{cm}^2 \tag{27}$$

where $A(V)$ is the total extinction in magnitudes and N_H is the hydrogen column density in cm^{-2} [18], if a charged particle with an imaginary refractive index has opacity within a few orders of magnitude of neutral hydrogen, it is evident the photon energy removed is negligible and the impact from particles with negative permeability can be neglected. The permeability is then computed using the half of the plasma particles generating magnetic fields which add to the photon magnetic field.

Continuing with the Effective Medium Theory to determine the effective permeability of the medium with respect to a photon sourced from the galactic core, Equation (10) can be rearranged to yield

$$A = \frac{\pi\left(\frac{\lambda}{2\pi}\right)^2\lambda_{eff}}{4\cdot\frac{1}{e_{dens40}+e_{dens50}}} = 9.13\times10^{-27} \tag{28}$$

where λ_{eff} is set to the *Hα* wavelength with $\eta_{eff}\approx1$, the term $\frac{\lambda}{2\pi}$ is the radius of the photon soliton at the *Hα* wavelength and $e_{dens40}+e_{dens50}$ is the total electron density for the 2 RBWs in the overlap region. From Equation (9), the effective relative permeability μ_{r_eff} is then

$$\mu_{r\_eff} = A\cdot\mu_r + (1-A) = 1.007 \tag{29}$$

where μ_r is set to the value computed in Section 5.1. The effective refractive index η_{eff} with $\epsilon_r = 1$ is then $\eta_{eff} = \sqrt{\mu_{r\_eff}} = 1.0037$. If at the shock discontinuity interface the plasma medium has an abrupt transition to free space ($\eta = 1$), the amplitude of the reflection will be consistent with the reflection coefficient Γ_r defined by

$$\Gamma_r = \left(\frac{\eta_{eff}-\eta}{\eta_{eff}+\eta}\right)^2 = 3.4\times10^{-6}. \tag{30}$$

5.2. Plasma Permeability for Photons Sourced from Reflection

The reflected photon EM wave intensity I_{refl} can be determined from the pre-

viously calculated photon EM wave intensity from the galactic core reaching the overlapping region $I_{\gamma s}$ with the equation

$$I_{refl} = \Gamma_r \cdot I_{\gamma s}. \tag{31}$$

Then for the reflected wave, with reference to Figure 5(a), the electron magnetic flux density averaged over the period of photon/electron interaction is evaluated in two distinct regions, R1 and R2. The RBW expansion velocities from SN1 and SN2 are both v_{bw} = 8000 km·s^{-1} and the RBW mediums or widths are expanding at v_w = 800 km·s^{-1}.

Region R1 consists of electrons from SN1 and SN2 which requires B_{e_bw} to be evaluated separately for each set of electrons. Starting with SN2 where the electron is angling away from the reflected photon with $\phi = \frac{\pi}{3}$, Equations (16)-(19) are leveraged to compute B_{ebwsn2}. For SN1, where the electron is angling toward the reflected photon with $\phi = \frac{\pi}{4}$, the average electron magnetic flux density as a function of time t and position x from Equation (16) is rewritten to account for the change in photon direction as

$$B_{er\_bwysn1}(t,x) = \frac{\pi}{\lambda}\int_{-\frac{\lambda}{2\pi}}^{\frac{\lambda}{2\pi}} \frac{\mu_0 q_e v_{bw}}{4\pi\left(\left(x''\right)^2 + \left(y'\right)^2\right)} \sin\left(\operatorname{atan}\left(\frac{y'}{x''}\right) + \phi\right) \mathrm{d}y \tag{32}$$

where $x'' = x - \left(\lambda_{eff} - v_{bw} \cdot t \cdot \cos(\phi)\right)$ and $y' = y - v_{bw} \cdot t \cdot \sin(\phi)$ with same constraints as previously applied. The electron magnetic flux density averaged over the period of photon/electron interaction for the reflected photon wave is then given by

$$B_{er\_bwxysn1}(t) = \frac{1}{\lambda_{eff}}\int_{c_{eff}\cdot t}^{c_{eff}\cdot t+\lambda_{eff}} B_{er\_bwysn1}(t,x)\psi'\left(x - c_{eff}\cdot t\right)\mathrm{d}x \tag{33}$$

and

$$B_{e\_bwsn1} = \frac{c_{eff} - v_{bw}\cdot\cos(\phi)}{\lambda_{eff}}\int_0^{\frac{\lambda_{eff}}{c_{eff} - v_{bw}\cdot\cos(\phi)}} B_{er\_bwxysn1}(t)\mathrm{d}t. \tag{34}$$

The average Region R1 B_{e_bwR1} is computed using the electron density as weighting factor with

$$B_{e\_bwR1} = \frac{e_{dens50}}{e_{dens40} + e_{dens50}} B_{e\_bwsn1} + \frac{e_{dens40}}{e_{dens40} + e_{dens50}} B_{e\_bwsn2}. \tag{35}$$

Region R2 consists of electrons from only SN2 and the previously computed B_{e_bwsn2} is applicable, such that $B_{e\_bwR2} = B_{e\_bwsn2}$. Photons from the reflection passing from Region R1 to Region R2 travel through the tapered trailing edge of the RBW from SN1 which provides a gradual impedance transition with negligible reflections. Photons from the reflection exiting Region R2 travel through the leading edge of the RBW from SN2 which also has a tapered profile reflecting negligible energy as it expands in the absence of ambient pressure.

Returning to the reflection from the shock interface, the peak reflected photon

magnetic field intensity H_{prmax} and average photon magnetic flux density B_{pavg} are computed with reflection coefficient Γ_r applied to Equations (21) and (22).

With the values for B_{e_bwR1}, B_{e_bwR2} and B_{pavg}, the relative permeability for the reflected path in the Region R1 and the Region R2 is then computed with

$$\mu_{rR1} = \frac{B_{e\_bwR1}}{B_{pavg}} + 1 \quad \text{and} \quad \mu_{rR2} = \frac{B_{e\_bwR2}}{B_{pavg}} + 1, \tag{36}$$

and the reflected effective relative permeability μ_{r_eff} is then calculated with

$$A_{R1} = \frac{\pi\left(\frac{\lambda}{2\pi}\right)^2 \lambda_{eff}}{4 \cdot \frac{1}{e_{dens40} + e_{dens50}}} \quad \text{and} \quad A_{R2} = \frac{\pi\left(\frac{\lambda}{2\pi}\right)^2 \lambda_{eff}}{4 \cdot \frac{1}{e_{dens40}}} \tag{37}$$

where for Region R1

$$\mu_{r\_effR1} = A_{R1} \cdot \mu_{rR1} + \left(1 - A_{R1}\right) \tag{38}$$

and for Region R2

$$\mu_{r\_effR2} = A_{R2} \cdot \mu_{rR2} + \left(1 - A_{R2}\right). \tag{39}$$

The effective refractive index for the reflected photon wave in Region R1 and Region R2 with relative permittivity $\epsilon_r = 1$ is then

$$\eta_{effR1} = \sqrt{\mu_{r\_effR1}} \quad \text{and} \quad \eta_{effR2} = \sqrt{\mu_{r\_effR2}} \tag{40}$$

The effective refractive index for the reflected wave in the plasma medium is determined by sweeping the value of η_{eff} in the sequential calculations for Equations ((21), (22), (32)-(39), (14)) to converge with the value from equation (40). With the reflection coefficient Γ calculated from Equation (30), the reflected refractive index converges to $\eta_{effR1} = 3.0$ for Region 1 and $\eta_{effR2} = 2.7$ for Region 2.

5.3. Redshift and Relative Magnitude of Reflection

Replacing η_1 with η_{eff} in Equation (4) to solve for the reflection redshift z yields

$$z = \frac{v_w \cdot \left(\eta_{eff} - 1\right)}{c - v_w \cdot \eta_{eff}}. \tag{41}$$

Referencing **Figure 5(a)**, in Region R1 the medium expansion velocity v_{wR1} along the reflected photon path is related to the medium expansion velocity of the blast shell width of SN1 v_{wSN1} by the equation

$$v_{wR1} = \frac{v_{wSN1}}{\cos\left(\phi\right)}, \tag{42}$$

where with $v_{wSN1} = 800\ \mathrm{km \cdot s^{-1}}$ and $\phi = \frac{\pi}{4}$ yields $v_{wR1} = 1131\ \mathrm{km \cdot s^{-1}}$. In Region R2 the medium expansion velocity v_{wR2} along the reflected photon path is

computed based on the sum of trailing edge velocity of the SN1 BW v_{bwSN1T} and the leading edge velocity of the SN2 BW v_{bwSN2L} with equation

$$v_{wR2} = \frac{v_{bwSN1T}}{\cos(\phi_1)} + \frac{v_{bwSN2L}}{\cos(\phi_2)}, \tag{43}$$

where with $v_{bwSN1T} = 7200\ \text{km}\cdot\text{s}^{-1}$, $v_{bwSN2L} = 8000\ \text{km}\cdot\text{s}^{-1}$, $\phi_1 = \frac{\pi}{4}$ and $\phi_2 = \frac{\pi}{3}$ yields $v_{wR2} = 26180\ \text{km}\cdot\text{s}^{-1}$. As defined by Equation (42), SNBW geometries with larger angles for ϕ can significantly increase v_w which in turn drives up z for a given effective refractive index η_{eff}.

Substituting the values for v_w and η_{eff} computed for Regions R1 and R2 into Equation (41) results in a redshift of $z_{R1} = 0.01$ for Region R1 and $z_{R2} = 0.19$ for Region R2. The sequential redshifts combine to yield a net redshift of $z = 0.20$ for the reflected photon wave relative to the host galaxy. Since η_{eff} in Equation (41) is not near a resonance, the associated redshift is largely achromatic.

The magnitude difference between the reflection and the galactic core of **Figure 5(b)** is determined based on viewing the galaxy edge-on, as the reflection travels parallel to the galactic plane. Approximating the edge-on galactic core light as concentrated within area A_{gc} defined as a rectangle 26 k LY across and 1 k LY thick and assuming the star distribution is uniform such that the average face-on surface intensity I_{face} is defined by

$$I_{face} = \frac{L_{core}}{\pi(R_{core})^2}, \tag{44}$$

if the star field intensity mixed with dust and gas from the ISM is maintained from the edge, then the edge-on luminosity L_{edge} can be expressed

$$L_{edge} = I_{face} \cdot A_{gc} = 4.71\times10^{35}\ \text{W}. \tag{45}$$

Referring to **Figure 5(b)** the arc reflection of 30 degrees with respect to the focal plane as shown has a spherical surface formed from a SNe 50 k LY away and the arc reflection has an approximate surface area of $A_{aseg} = 5.8\times10^{39}\ \text{m}^2$. The reflection is sourced with light from the galactic core which passes through a central focal area spaced 25 k LY away in the direction of the galaxy center. The central focal area can be approximated by the intersection formed by a projection of the reflection surface area to a point 50 k LY below the galaxy center with a focal plane positioned 25 k LY below the reflection and parallel to the galactic core. The intersection traces out a focal plane surface area $A_{fp} = \frac{A_{aseg}}{\left(\frac{50}{25}\right)^2} = 1.46\times10^{39}\ \text{m}^2$. The focal plane surface area is 10 k LY above the galactic core and the projection continues onto the galactic core to trace out a central source region with surface area of $A_{gcfa} = \frac{A_{aseg}}{\left(\frac{50}{15}\right)^2} = 5.26\times10^{38}\ \text{m}^2$. The luminosity of the galactic core region

sourcing the reflection can be approximated by $L_{gcsa} = I_{face} \cdot A_{gcfa} = 1.06 \times 10^{35}$ W. Then the total luminosity from the source area incident on the arc segment can be computed by the amount of galactic core source area luminosity passing through the focal surface area A_{fp} at H = 10 k LY above the galactic core as $L_{ainc} = L_{gcsa} \cdot \frac{A_{fp}}{4\pi H^2} = 1.38 \times 10^{33}$ W.

The reflected luminosity of the arc segment L_{arefl} can then be expressed

$$L_{arefl} = L_{ainc} \cdot \Gamma_r \cdot G_{sph} = 4.7 \times 10^{29} \text{ W}, \tag{46}$$

where Γ_r is from Equation (29) and the term G_{sph} factors in 20 dB gain which is typical for a spherical reflector. If the arc spans 60 degrees, the luminosity L_{arefl} will increase by an approximate factor of 2.

The observed magnitude difference between the reflection from the 60 degree arc and the edge-on galactic core is then

$$\Delta m = -2.5 \log_{10} \left(\frac{2 \times L_{arefl}}{L_{edge}} \right) = +14.3 . \tag{47}$$

This value for Δm is in the range of the magnitude difference between the moon and the sun.

5.4. Gravitational Lenses with Triple and Quadruple Images

The Hubble Space Telescope and Webb Space Telescope have captured gravitational lenses where multiple images are formed around a central galaxy. A quadruple imaged lens, referred to as an Einstein Cross [19], is shown to be formed from 4 intersecting RBWs where the quadruple image is comprised of redshifted reflected light from the central galaxy.

Figure 6(a) is a Hubble Space Telescope image of Einstein Cross WGD-J0405-3308 which is considered the front view orientation. **Figure 6(b)** is a top view of the structure showing two of the four RBWs with one positioned in front and one behind the central elliptical galaxy. The overlap of the SN1 and SN2 blast waves form a ring in **Figure 6(c)**, which also shows the positions of SN3 and SN4. In **Figure 6(d)**, the blast waves from SN3 and SN4 are shown in vertical crosshatch. The intersection of the ring from SN1 and SN2 with the spherical blast waves from SN3 and SN4 form 4 shocked overlapping regions as shown with triple the plasma density of a single blast wave, which creates the bright reflections at the Einstein Cross points. Note that the rectangular cross section of the dark shaded triple overlap regions in **Figure 6(d)** are partially visible in **Figure 6(a)**. **Figure 6(e)** is a Hubble Space Telescope image of an Einstein Cross configuration found in galaxy cluster J2211-0350 [20]. **Figure 6(f)** is a top view of the structure which includes the central elliptical galaxy and the position of SN1 and its associated blast wave. **Figure 6(g)** is a front view which includes the positions of SN2, SN3 and SN4 around the galaxy. In **Figure 6(h)**, the blast waves of SN2, SN3 and SN4 are added. The blast waves from SN2 and SN3 intersect to form an overlap ring. This ring intersects the spherical blast wave

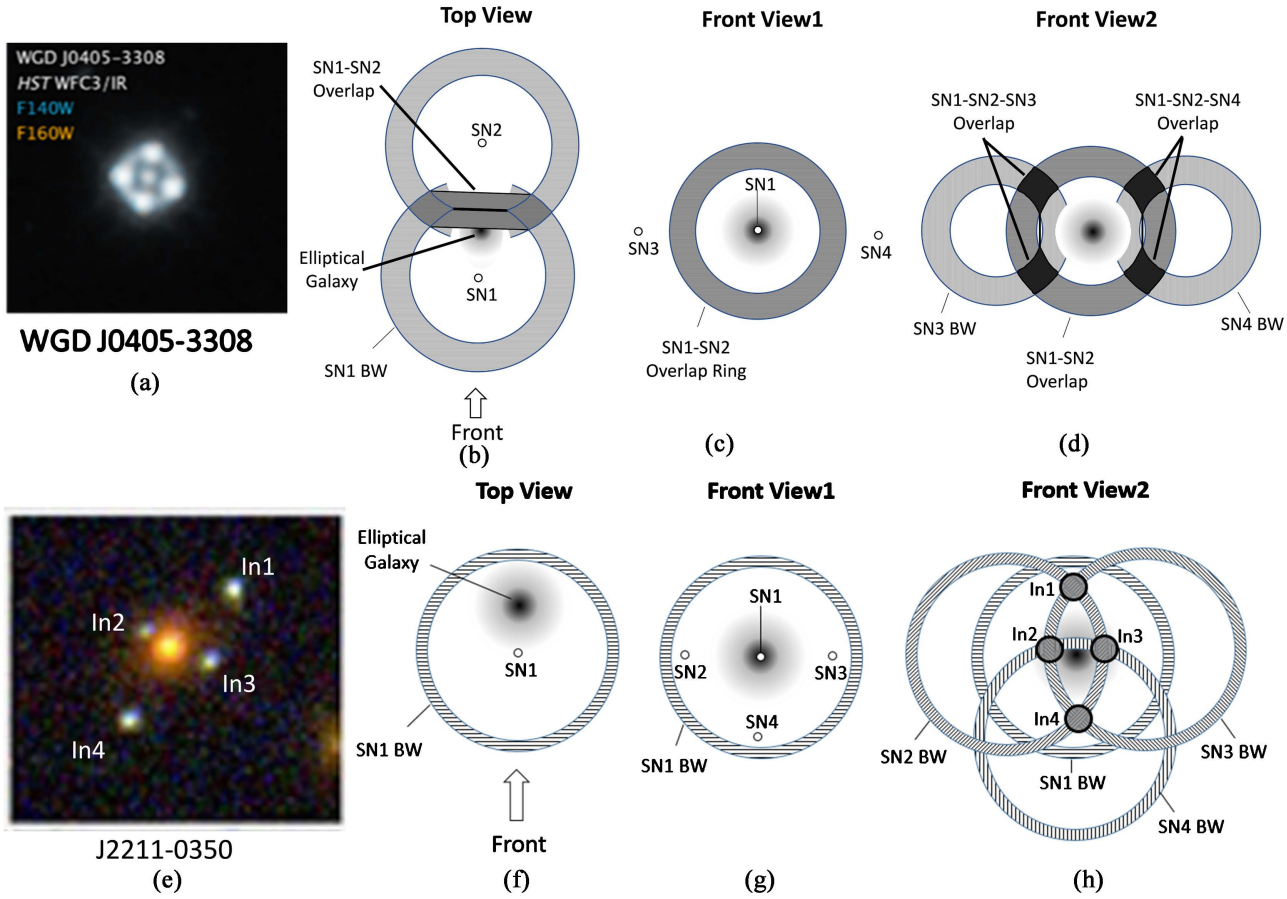

Figure 6. Gravitational Lens images and underlying BWs. (a) Image of Einstein Cross WGD J0405-3308. (b) & (c) Top and front view of intersection ring formed from SN1 and SN2. (d) Triple intersections of blast waves SN1 - SN4 forming the Einstein Cross pattern in dark grey. (e) Image J2211-0350 with Einstein Cross. (f) & (g) Top and front view of SN1 blast wave. (h) Triple intersections of blast waves forming the Einstein Cross pattern points In1-In4.

from SN1 at the far side of the elliptical galaxy at intersection points In1 and In4. Similarly, the blast waves from SN2 and SN4 and the blast waves from SN3 and SN4 form rings which intersect with SN1's blast wave at points In3 and In2, respectively. The intersections In1 to In4 are each comprised of 3 blast waves with triple the plasma density of a single blast wave, driving bright reflections from the outer shocked surface of SN1's blast wave which forms the Einstein Cross points.

Figure 7(a) is a Webb Space Telescope image of a triple imaged galaxy found in Galaxy Cluster RX J2129 (https://esawebb.org/images/potm2302a/). Each of the 3 images is from a different perspective with the galaxy arms inverted in two images. Figure 7(b) is depiction of underlying RBWs capable of generating specular reflections where the SN for RBW2 exploded first and may have later triggered the SNs for RBW1 and RBW3. For the larger diameter RBW2, the host galaxy is less than the focal length away resulting in a noninverted reflection and for RBWs 1 and 3 the host galaxy is beyond the focal length away (f1 and f3), resulting in inverted reflections. The depiction predicts one of the bright foreground galaxies is the spiral host galaxy sourcing the reflected images. Alternatively,

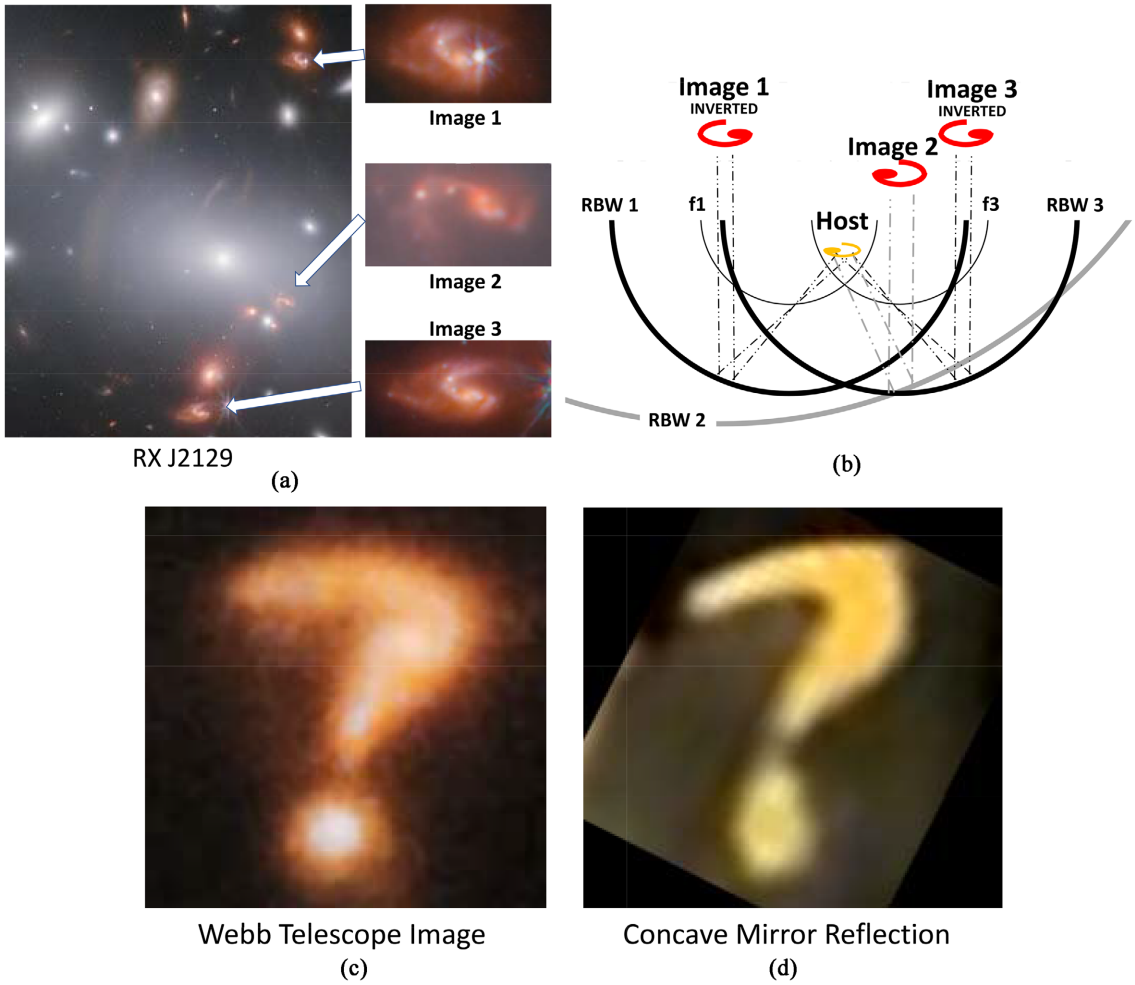

Figure 7. Gravitational Lens images. (a) Triple imaged galaxy found in galaxy cluster RX J2129. (b) Depiction of underlying blast waves generating 3 equivalent perspectives of imaged galaxy. (c) "Cosmic Question Mark" image captured by the Webb Telescope (d) Distorted image of an ellipse positioned across the focal point of a concave mirror.

multiple images could be generated with a single RBW which encounters an inhomogeneous IGM creating spherical surface distortions similar to those seen with the Sunburst Arc (https://esahubble.org/images/heic1920b/) and SN remnant SN1006 (https://hubblesite.org/contents/media/images/2008/22/2351-Image.html). **Figure 7(c)** from the Webb Telescope resembles a giant question mark which was captured in the background of an image featuring the stars Herbig-Haro 46/47 (https://www.space.com/james-webb-space-telescope-question-mark-galaxy-photo). **Figure 7(d)** shows a similar image sourced from a reflection formed by positioning a printed paper ellipse off-axis across the focal point of an optically true concave mirror. The set up emulates an RBW reflection from an elliptical galaxy or tilted spiral galaxy positioned near the RBW focal point.

6. The Hubble Equation

Application of the RBW electrodynamic properties to incoming extragalactic

light fields exhibits redshift characteristics similar to the Hubble Law

$$H_0 = \frac{v_r}{d} \tag{48}$$

where H_0 is the Hubble constant, v_r is the recession velocity and d is the distance to an observed extragalactic object. The recession velocity v_r can be expressed

$$v_r \cong c \cdot z\,. \tag{49}$$

Equation (49) can be expanded in terms of the SN blast wave parameters leveraging Equation (41)

$$z = \frac{v_w \cdot \left(\eta_{eff} - 1\right)}{c - v_w \cdot \eta_{eff}}, \tag{41}$$

and substituting η_{eff} as a function of distance d in Mpc using Equations (7), (9) and (14) to yield

$$v_r\left(d\right) = \frac{c \cdot v_w \cdot \left(\left(A \cdot \left(\frac{B_{e\_bw}}{B_{pavg}\left(d\right)} + 1\right) + \left(1 - A\right)\right)^{\frac{1}{2}} - 1\right)}{c - v_w \cdot \left(A \cdot \left(\frac{B_{e\_bw}}{B_{pavg}\left(d\right)} + 1\right) + \left(1 - A\right)\right)^{\frac{1}{2}}} \mathrm{m \cdot s^{-1}}, \tag{50}$$

where

$$B_{pavg}\left(d\right) = \frac{2 \cdot \mu_0}{\lambda} \cdot \int_0^{\frac{\lambda}{2}} \left(\frac{2 \cdot P_{\gamma s} \cdot \left(1 - a_{dust}\right)^d}{4 \cdot \pi \cdot \left(d \cdot 3.26 \times 10^6 \cdot LY\right)^2 * Z_0}\right)^{\frac{1}{2}} \cdot \sin\left(2\pi \frac{x}{\lambda}\right) \mathrm{d}x\,. \tag{51}$$

The term a_{dust} is the average factor of photon soliton intensity lost per Mpc due to intergalactic dust attenuation.

The plots of Figure 8 have been generated by loading Equations (50) and (51) with exemplary parameters $v_w = 8000\ \mathrm{km \cdot s^{-1}}$, $A = 2 \times 10^{-28}$ and

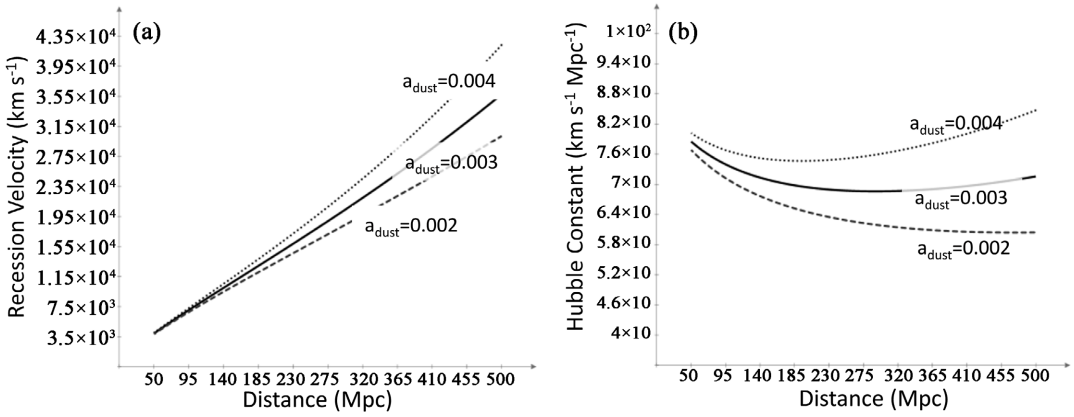

Figure 8. Plots of Plasma-Based Equations for Recession Velocity and Hubble Constant. (a) Recession Velocity vs. Distance plots for multiple dust attenuation factors. (b) Hubble Constant vs. Distance plots for multiple dust attenuation factors.

$B_{e\_bw} = 6.8\times10^{-7}$ T to demonstrate the characteristics of the plasma-induced redshift over a wide range of distances for a single RBW around the galaxy.

Figure 8(a) shows a plot of the recession velocity vs. distance and Figure 8(b) the Hubble Constant vs. distance defined by

$$H_0(d) = \frac{v_r(d)}{d} \tag{52}$$

with the intergalactic dust attenuation factor set to 0.002, 0.003 and 0.004. The impact of intergalactic dust can be seen where a_{dust} can be adjusted along with other parameters to better align the Hubble Constant H_0 estimates for both early time and late time observation campaigns. Figure 8(b) shows an increase in the computed Hubble Constant with reduced distance. At distances below the 100 Mpc range, the measured Hubble Constant can include significant contributions from non-Hubble flow related sources, such as galactic peculiar velocities, local universe 3D bulk flow velocity fields, standard candle statistical errors and estimated dust-related attenuation errors [21] [22]. Estimates for variables impacting the distance ladder have been refined over time and are aligned to support a fixed Hubble Constant. The exemplary parameters used in Equations (50) and (51) imply a low density RBW with high leading-edge velocity and low trailing-edge velocity. While the single RBW equation can emulate the Hubble observations with various parameter sets, the local IGM would require multiple overlapping RBWs for full sky region coverage.

7. Discussion and Conclusion

The analysis demonstrates relativistic RBWs generate magnetic fields which influence the propagation of EM waves. The dominant mechanism driving up the plasma permeability is the particle velocity imparted by the SNe, where during the period a particle crosses the path of a photon soliton it partially transits the photon introducing an offset magnetic field in-phase with the photon. When RBWs intersect, the discontinuity in permeability across the shocked surface reflects light from the host galaxy exposing the overlapping blast wave sections which naturally form rings, arcs or Einstein Crosses. The permeability of the expanding blast wave shells is shown to redshift the reflected light consistent with the measured light spectrum of these structures. Einstein Cross structures and a triple-imaged galaxy provide evidence supporting the analysis as these are naturally formed by SN blast waves.

Equations for the plasma permeability rely on a coherent photon soliton wave interacting with a high-velocity low-density plasma spread out over thousands of light years. As the computed plasma effective index of refraction is dependent on the photon amplitude but not the number of photons, objects with wide-ranging intensity at the same distance may be observed with the same redshift. The resultant redshift is governed by factors impacting the path loss from the source, such as attenuation due to distance and dust. High velocity plasma interactions may be responsible for other cosmic phenomena such as the Lyman-Alpha For-

est. Multiple researchers have reported electrons bound to ions can drive up the permittivity in many ionic plasmas and for photon energies from the optical to soft x-rays, drive the refractive index greater than 1 [23]. The observed narrowband permittivity characteristics in a relativistic plasma could modulate the refractive index and displace narrow frequency bands in the optical spectrum. In the Milky Way, a multi-RBW 3D Hubble equation could be derived leveraging sky-region-based observations to identify potential RBW locations in the local IGM.

Conflicts of Interest

The author declares no conflicts of interest regarding the publication of this paper.

References

[1] Hillebrandt, W. and Niemeyer, J.C. (2000) Type Ia Supernova Explosion Models. *Annual Review of Astronomy and Astrophysics*, **38**, 191-230. https://doi.org/10.1146/annurev.astro.38.1.191

[2] Hoflick, P. and Khokhlov, A. (1996) Explosion Models for Type IA Supernovae: A Comparison with Observed Light Curves, Distances, H_0, and Q_0. *Astrophysical Journal*, **457**, 500-528. https://doi.org/10.1086/176748

[3] Haid, S., Walch, S., Naab, T., Seifried, D., Mackey, J. and Gatto, A. (2016) Supernova-Blast Waves in Wind-Blown Bubbles, Turbulent, and Power-Law Ambient Media. *Monthly Notices of the Royal Astronomical Society*, **460**, 2962-2978. https://doi.org/10.1093/mnras/stw1082

[4] Freidlander, F.G. (1946) The Diffraction of Sound Pulses I. Diffraction by a Semi-Infinite Plane. *Proceedings of the Royal Society of London*, **186**, 322-344. https://doi.org/10.1098/rspa.1946.0046

[5] Gurnett, D.A. and Bhattacharjee, A. (2017) Introduction to Plasma Physics. Cambridge University Press, Cambridge.

[6] Krick, J.E. and Bernstein, R.A. (2007) Diffuse Optical Light in Galaxy Clusters. II. Correlations with Cluster Properties. *The Astrophysical Journal*, **134**, 466-493. https://doi.org/10.1086/518787

[7] Palladino, L.E., Holley-Bockelmann, K., Morrison, H., Durrell, P.R., Ciardullo, R., Feldmeier, J., Wade, R.A., Kirkpatrick, J.D. and Lowrance, P. (2012) Identifying High-Metallicity M Giants at Intragroup Distances with Sloan Digital Sky Survey. *The Astrophysical Journal*, **143**, 128-136. https://doi.org/10.1088/0004-6256/143/6/128

[8] Li, M., Bryan, G.L. and Ostriker, J.P. (2017) Quantifying Supernovae-Driven Multiphase Galactic Outflows. *The Astrophysical Journal*, **841**, 101-116. https://doi.org/10.3847/1538-4357/aa7263

[9] Klopfenstein, R.W. (1956) A Transmission Line Taper of Improved Design. *Proceedings of the IRE*, **44**, 31-35. https://doi.org/10.1109/JRPROC.1956.274847

[10] Inan, U.S. and Golkowski, M. (2011) Principles of Plasma Physics for Engineers and Scientists. Cambridge University Press, Cambridge.

[11] Cui, T.J., Tang, W.X., Yang, X.M., Mei, Z.L. and Jiang, W.X. (2016) Metamaterials. CRC Press, Boca Raton.

[12] Roychoudhuri, C., Kracklauer, A.F. and Creath, K. (2008) The Nature of Light. CRC

Press, Boca Raton.

[13] Draine, B.T. and McKee, C.F. (1993) Theory of Interstellar Shocks. *Annual Review of Astronomy and Astrophysics*, **31**, 373-432. https://doi.org/10.1146/annurev.aa.31.090193.002105

[14] Ofek, E.O., Rix, H.-W. and Maoz, D. (2003) The Redshift Distribution of Gravitational Lenses Revisited: Constraints on Galaxy Mass Evolution, *Monthly Notices of the Royal Astronomical Society*, **343**, 639-652. https://doi.org/10.1046/j.1365-8711.2003.06707.x

[15] Fukugita, M., Futamase, T., Kasai, M. and Turner, E.L. (1992) Statistical Properties of Gravitational Lenses with a Nonzero Cosmological Constant. *The Astrophysical Journal*, **393**, 3-21. https://doi.org/10.1086/171481

[16] Branch, D. and Wheeler, J.C. (2017) Supernova Explosions. Springer, Berlin.

[17] Flynn, C., Holmberg, J., Portinari, L., Fuchs, B. and Jahrei, B.H. (2006) On the Mass-to-Light Ratio of the Local Galactic Disc and the Optical Luminosity of the Galaxy. *Monthly Notices of the Royal Astronomical Society*, **372**, 1149-1160. https://doi.org/10.1111/j.1365-2966.2006.10911.x

[18] Weingartner, J. and Draine, B.T. (2001) Dust Grain-Size Distributions and Extinction in the Milky Way, Large Magellanic Cloud, and Small Magellanic Cloud. *The Astrophysical Journal*, **548**, 296-309. https://doi.org/10.1086/318651

[19] Nierenberg, A.M., Gilman, D., Treu, T., Brammer, G., Birrer, S., Moustakas, L., Agnello, A., Anguita, T., Fassnacht, C.D., Motta, V., Peter, A.H.G. and Sluse, D. (2019) Double Dark Matter Vision: Twice the Number of Compact-Source Lenses with Narrow-Line Lensing and the WFC3 Grism. *Monthly Notices of the Royal Astronomical Society*, **492**, 5314-5335. https://doi.org/10.1093/mnras/stz3588

[20] Bettoni, D., Falomo, R., Scarpa, R., Nagrello, M., Omizzolo, A., Corradi, R.L.M., Raverte, D. and Vulcani, B. (2019) A New Einstein Cross Gravitational Lens of a Lyman-Break Galaxy. *The Astrophysical Journal Letters*, **873**, L14. https://doi.org/10.3847/2041-8213/ab0aeb

[21] Li, N., Li, C., Mo, H., Hu, J., Zhou, S. and Du, C. (2020) Estimating Dust Attenuation from Galactic Spectra. I. Methodology and Tests. *The Astrophysical Journal Letters*, **896**, 38-60. https://doi.org/10.3847/2041-8213/ab0aeb

[22] Hoffman, Y., Courtois, H.M. and Tully, R.B. (2015) Cosmic Bulk Flow and the Local Motion from Cosmicflows-2. *Monthly Notices of the Royal Astronomical Society*, **449**, 4494-4505. https://doi.org/10.1093/mnras/stv615

[23] Nilsen, J. and Johnson, W.R. (2005) Plasma Interferometry and How the Bound-Electron Contribution Can Bend Fringes in Unexpected Ways. *Applied Optics*, **44**, 7295-7301. https://doi.org/10.1364/AO.44.007295